

Stress decomposition in LAOS of dense colloidal suspensions

Edward Y. X. Ong, Meera Ramaswamy, Ran Niu, Neil Y. C. Lin, Abhishek Shetty, Roseanna N. Zia, Gareth H. McKinley, and Itai Cohen

Citation: *Journal of Rheology* **64**, 343 (2020); doi: 10.1122/1.5144520

View online: <https://doi.org/10.1122/1.5144520>

View Table of Contents: <https://sor.scitation.org/toc/jor/64/2>

Published by the [The Society of Rheology](#)

ARTICLES YOU MAY BE INTERESTED IN

[Preface: Physics of dense suspensions](#)

Journal of Rheology **64**, 223 (2020); <https://doi.org/10.1122/8.0000016>

[Shear thickening in dense non-Brownian suspensions: Viscous to inertial transition](#)

Journal of Rheology **64**, 227 (2020); <https://doi.org/10.1122/1.5129680>

[Experimental test of a frictional contact model for shear thickening in concentrated colloidal suspensions](#)

Journal of Rheology **64**, 267 (2020); <https://doi.org/10.1122/1.5129798>

[Elasticity and plasticity of highly concentrated noncolloidal suspensions under shear](#)

Journal of Rheology **64**, 469 (2020); <https://doi.org/10.1122/1.5115558>

[Fluctuations at the onset of discontinuous shear thickening in a suspension](#)

Journal of Rheology **64**, 309 (2020); <https://doi.org/10.1122/1.5131740>

[Investigating the nature of discontinuous shear thickening: Beyond a mean-field description](#)

Journal of Rheology **64**, 329 (2020); <https://doi.org/10.1122/1.5132317>



DISCOVER the **RHEOMETER** with the...
Sensitivity • Ease-of-use • Versatility
to address the most **demanding** applications

The **NEW Discovery Hybrid Rheometer**





Stress decomposition in LAOS of dense colloidal suspensions

Edward Y. X. Ong,^{1,a)} Meera Ramaswamy,² Ran Niu,² Neil Y. C. Lin,^{2,b)} Abhishek Shetty,³ Roseanna N. Zia,⁴ Gareth H. McKinley,⁵ and Itai Cohen²

¹*Department of Applied Engineering and Physics, Cornell University, Ithaca, New York 14850*

²*Department of Physics, Cornell University, Ithaca, New York 14850*

³*Department of Rheology, Anton Paar USA, Ashland, Virginia 23005*

⁴*Department of Chemical Engineering, Stanford University, Stanford, California 94305*

⁵*Department of Mechanical Engineering, Massachusetts Institute of Technology, Cambridge, Massachusetts 02139*

(Received 1 January 2020; final revision received 28 January 2020; published 4 March 2020)

Abstract

We present a method for stress decomposition to understand the rich interactions present in the large amplitude oscillatory shear (LAOS) of shear-thickening suspensions. This method is rooted in experiments, does not rely on a preexisting rheological model, and is free of any *a priori* symmetry arguments. The decomposition allows us to extract the hydrodynamic, contact, and Brownian contributions to map out how these stresses evolve over an oscillation cycle. Access to the time evolution of each stress component provides us with valuable insights into the microscopic details governing the system rheology such as the identification of the time scale for buildup and relaxation of the force chains governing suspension thickening, as well as various asymmetries characterizing the microstructure. While we have chosen to demonstrate this technique on colloidal suspensions, its generality should allow us to utilize it to investigate the LAOS response of other systems ranging from colloidal gels to polymer melts. © 2020 The Society of Rheology. <https://doi.org/10.1122/1.5144520>

I. INTRODUCTION

Large amplitude oscillatory shear (LAOS) has, in recent years, emerged as a powerful method for characterizing the nonlinear rheological response of materials [1–10]. In this method, a sample undergoes oscillatory shear in which the strain amplitude, γ_0 , is large (usually $\gamma_0 > 100\%$). Wide adoption of this technique stems from its versatility and ease of implementation in most conventional rheometers. By varying the oscillation amplitude in a systematic way, it is possible to map out both the linear and nonlinear responses of a material. We show a typical set of LAOS plots for shear-thickening fluids and Newtonian fluids in Fig. 1. For a Newtonian fluid, the stress-strain plot is circular, while the stress-strain rate plot is linear (dashed lines in Fig. 1). For shear thickening fluids, there are obvious deviations from the Newtonian response, especially at the onset of thickening near the extreme strains. While LAOS experiments characterize these deviations, they do not shed light on their origins. Thus, it remains challenging to interpret the results, in part, because the measured stress in these experiments can arise from a variety of microscale mechanisms.

To address this challenge, pioneering studies have developed a number of theoretical approaches [2,9,11–19]. The most powerful approach for interpreting the data is to have a

constitutive equation that relates the measured stress to physical properties of the material such as the viscosity and modulus [2,9,12–15]. Such relations, however, are often incomplete, especially in highly nonlinear materials [13–15]. More commonly, theorists have tried to construct phenomenon-specific theoretical models based on intuition about the microscale dynamics governing the material response. Unfortunately, for many fluids, including shear-thickening suspensions, such models have not yet been fully developed due to insufficient understanding of the microscale dynamics. To address this gap, researchers often turn to numerical simulations to determine the dominant microscopic mechanisms at play. The computational cost, however, of including all possible mechanisms, or at least a subset of known microscopic forces, is often prohibitive. Thus, researchers must pick and choose what mechanisms to incorporate in the simulations, which, in some cases has, led to simulations missing a dominant mechanism. Because of these limitations, even simulations constructed to capture the total stress response often do not accurately account for the relative stress contributions of the various microscale processes determining the system rheology [20].

Outside of theory and simulations, there have been attempts to experimentally understand the physics encoded in LAOS deformation without assuming any constitutive form. One such approach is recovery rheology, in which the sample undergoes shear stress cessation/recoil at various points on the LAOS cycle to extract the recoverable strain [21–23]. The success of this approach in improving our understanding of the physics of polymeric systems suggests that carefully planned, time-dependent experimental protocols can be a powerful method to understand the complex physics involved in these nonlinear flows.

Note: This paper is part of the special issue on Physics of Dense Suspensions.

^{a)}Author to whom correspondence should be addressed; electronic mail: eo263@cornell.edu

^{b)}Present address: Department of Mechanical and Aerospace Engineering, University of California, Los Angeles, CA 90095.

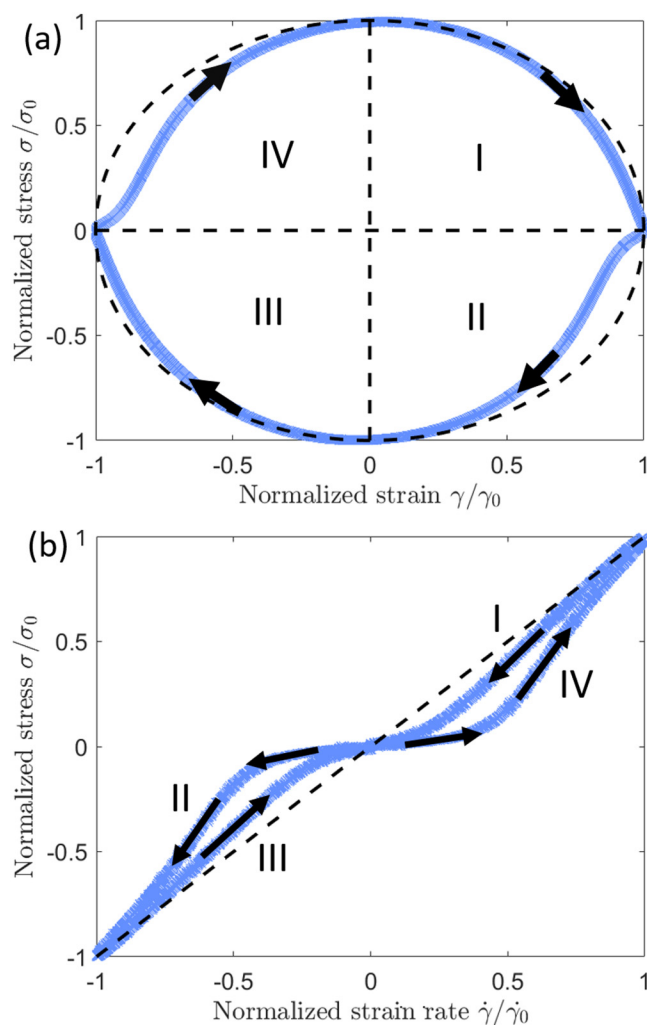


FIG. 1. Different ways of visualizing the LAOS cycle for a shear-thickening colloidal suspension. The stress, strain, and the strain rate are normalized by their maximum values, σ_0 , γ_0 , and $\dot{\gamma}_0$, respectively. The arrows indicate the direction in which the curve is traversed. The normalized stress versus strain Lissajous–Bowditch curve in (a) is divided into four quadrants for the ease of reference. The corresponding regions in the normalized stress versus strain rate curve in (b) are similarly labeled. The dashed lines in (a) and (b) correspond to Newtonian behavior, respectively.

Here, we present a set of experimental protocols to improve the interpretability of LAOS measurements through complete decomposition of the measured stress into its constituent components. We show that for dense suspensions, conducting shear reversal and shear cessation experiments at each point along a LAOS cycle allows for determining the relative contributions of the contact, Brownian, and hydrodynamic stresses. Resolving the total stress into its components provides insights into the dominant physical processes governing the response, accurately characterizes their evolution, and can serve to more rigorously test model predictions.

II. BACKGROUND

It has previously been shown that the total shear stress of a suspension of frictional but otherwise hard microspheres suspended in a Newtonian fluid under an imposed shear flow is

well modeled as a linear sum of contact (C), Brownian (B), and hydrodynamic (H) stresses [24–30],

$$\sigma_T = \sigma_C + \sigma_B + \sigma_H. \quad (1)$$

Here, the Brownian stresses arise from thermal agitation of the particles and the anisotropy in their distributions [31]. During shear, the particle distribution is compressed along the maximal compression axis and the Brownian stresses oppose this compression. The hydrodynamic stresses arise from the viscous damping of the solvent and depend both on the local particle velocities and global configuration of the suspension [32,33]. This stress is proportional to the applied strain rate.

The contact stress, σ_C , has been observed to arise when particles in dense suspensions are sufficiently strained, resulting in tight packing along the maximum compressive axis. Typical contributions to σ_C arise from interparticle normal forces and friction [34–36]. The exact origin and balance of these contributions is an active area of study and may depend on the specifics of the suspension chemistry. In all of these cases, however, the contact stresses rapidly diminish with increasing particle separation, characterized by a decay length scale typically much smaller than that of other stresses.

In a previous work, it was shown that the contact stress of a shear-thickening colloidal suspension can be distinguished from the hydrodynamic stress by conducting a reversal experiment [37]. In those experiments, the flow was very strong compared to Brownian motion, as characterized by the Péclet number, $Pe = \dot{\gamma}a^2/D \sim 10^5$, where $\dot{\gamma}$ is the shear rate, a is the particle size, and $D = k_B T / 6\pi\eta a$ is the characteristic diffusivity of a single particle. As a consequence, the Brownian contribution was thought to be negligible and $\sigma_T = \sigma_C + \sigma_H$. Non-Brownian simulations of the reversal experiment in the same study that included contact stresses were found to be in excellent agreement with the reversal experiments capturing both the thickening during continuous shear as well as the changes in the total stress after reversal. These simulations confirmed that just after reversal the magnitude of the hydrodynamic contribution to the stress, σ_H , was unchanged while the contact contribution, σ_C , decayed to zero. The contact stress can thus be determined by subtracting the remaining stress immediately after reversal, which corresponds to σ_H , from σ_T . These results confirm the guiding principle behind this technique that low Reynolds number flows have time-reversal symmetry so that their magnitude before and after reversal remains unchanged while the contact stresses vanish [38,39].

For flows characterized by moderate Péclet numbers, the situation is more complicated since Brownian stresses play a role and are coupled to the hydrodynamic forces. Here, Brownian stresses due to the suspension densification along the maximum compressive axis contribute to the total stress as given by Eq. (1). Upon reversal of a thickened suspension, while the hydrodynamic stress has the same magnitude but *opposite direction*, the Brownian stress maintains both the same magnitude *and the same direction*. Thus, reversal experiments alone cannot determine the exact hydrodynamic stress since the stress immediately after reversal, $\sigma_{rev,t}$ is the difference between the hydrodynamic and Brownian stresses

prior to reversal,

$$\sigma_{\text{rev}} = \sigma_H - \sigma_B. \quad (2)$$

More information about the relative contributions of the stresses can be obtained by a shear cessation experiment. In this experiment, the suspension flow is halted by rapidly reducing the strain rate to zero. The hydrodynamic stress (σ_H), which is rate-dependent, immediately decays to zero while the elastic components due to contact (σ_C) and Brownian (σ_B) stresses remain unchanged immediately after cessation [40–48]. Often, contact stresses due to particle elasticity or electrostatic repulsion decay too rapidly to measure using conventional rheometers. The contribution from Brownian stresses due to the asymmetry in particle distribution, however, decays over a much longer time scale. In principle, therefore, it should be possible to determine σ_B from a cessation experiment by extrapolating the stress after cessation to the value at the point of cessation. Equation (2) then allows us to determine σ_H from the shear reversal experiment, which subsequently allows us to determine σ_C from Eq. (1). Thus, by separately conducting a shear reversal and shear cessation experiment at each point along the LAOS Lissajous–Bowditch curve, we can extract the relative contributions of σ_C , σ_B , and σ_H .

III. EXPERIMENTAL METHODS

A. Materials

We carry out the measurements on a canonical shear-thickening suspension of charge-stabilized silica (Angstrom Sphere) with a radius of 2 μm suspended in pure glycerol (Sigma Aldrich, $\eta_0 = 7 \text{ Pa s}$ at 3.5 $^\circ\text{C}$) at a volume fraction $\phi = 0.48$. The suspension was prepared using simple mixing and sonication. Since glycerol is hygroscopic, contact with the environment was kept to a minimum by sealing vials with parafilm tape, and each sample was freshly prepared prior to measurement. We found that the rate dependent viscosity of the suspension was highly consistent and varied by less than 5% for each sample throughout the measurements, indicating absorption of water into the sample was minimal. This is, in part, due to the low surface area to volume ratio of the Couette geometry. Importantly, the high viscosity lowers the critical strain rate required for thickening and provides a longer time window for conducting our reversal and cessation experiments. Over the range of strain rates used in the experiments, we observed no secondary flows, squeeze flow, Taylor vortices, or other nonlinear rheological behavior that could affect our results.

B. Measurement apparatus and specifications

Measurements were performed using the ARES-G2 strain-controlled rheometer with a Couette cell. The effective bob length is 41.5 mm, and the inner and outer diameters are 27.7 mm and 30.0 mm, respectively, which correspond to a gap ratio of 0.91. The sample was maintained at a temperature of 3.5 $^\circ\text{C}$ using a Peltier temperature controller. The range of strain rates used in our measurements is $0.05 \text{ s}^{-1} < \dot{\gamma} < 1 \text{ s}^{-1}$ corresponding to a Péclet number range of $10^4 < \text{Pe} < 10^5$

and a Reynolds number range of $10^{-7} < \text{Re} < 10^{-6}$, where we set the characteristic length scale as the particle radius and the characteristic velocity as $\dot{\gamma}L$, where L is the gap width. When recording the stress at a frequency of 250 Hz, the rheometer has a noise floor of $\sim 0.1 \text{ Pa}$ and a strain rate resolution of 10^{-4} s^{-1} .

Because the rheometer resolution is limited by the finite motor adjustment time and delay in the transducer dynamics, care must be taken when collecting data for reversal and cessation protocols. The instrument limitations are evident by the inertial overshoot in the instantaneous strain rate immediately after imposing the step change at reversal and cessation. The time taken for the instrument to correct for this overshoot was characterized using pure glycerol (see supplementary material [51]). We found that this response time increases with instantaneous strain rate and disappears after 20–70 ms for the range of parameters in our experiments. In our results for the reversal experiments, we only plot data at strains where the instantaneous strain rate has reached a steady state. For the cessation experiment, we indicate the instrument response time as a gray shaded region and use the data at longer time scales to conduct our analysis.

The same protocol has been performed on an Anton Paar MCR702 rheometer with a Couette cell, which has a gap ratio of 0.92 (see supplementary material [51]). Here, we present data gathered using the ARES rheometer since it had better resolution for the estimation of Brownian stresses given its faster response time following shear cessation.

C. Measurements

1. Visualization of LAOS response using Lissajous–Bowditch curves

The LAOS curves used in this paper are parameterized by a strain amplitude, $\gamma_0 = 5$ and a frequency $\omega = 0.2 \text{ s}^{-1}$, which gives a strain rate amplitude $\dot{\gamma}_0 = 1 \text{ s}^{-1}$. These parameters were chosen to ensure the strain and strain rate amplitudes are large enough to induce thickening behavior in the suspension. The stress, strain, and the strain rate are normalized by their maximum values, σ_0 , γ_0 , and $\dot{\gamma}_0$, respectively, and we plot the normalized stress against normalized strain in Fig. 1(a) and the normalized stress against normalized strain rate in Fig. 1(b). In this representation, the response of a Newtonian fluid corresponds to a circle in the stress-strain plot and a line in the stress-strain rate plot. Deviations from these forms indicate non-Newtonian behavior.

The LAOS curves for our suspension show significant deviations from the linear viscous behavior (solid versus dashed lines in Fig. 1). These deviations are especially prominent near the large strains corresponding to an instantaneous strain rate of zero. To analyze these deviations, we divide the Lissajous–Bowditch curves into four quadrants. Moving clockwise, quadrant I shows small deviations from the linear response indicating that the system is behaving like a Newtonian fluid with a high shear-thickened viscosity. From the stress-strain rate curve [Fig. 1(b)], we also find a small region where the slope is smaller than one indicating that the suspension thins near the transition to quadrant II. At the crossover between quadrants I and II, the instantaneous strain

rate changes direction and the strain starts to decrease. From the stress versus strain rate curve [Fig. 1(b)] for quadrant II, we observe shear thinning (slope < 1) followed by shear thickening (slope > 1). The thickened state is maintained through the crossover to quadrant III, which is mirror symmetric to quadrant I. Due to the mirror symmetry of quadrants I and III and quadrants II and IV, it is sufficient to analyze just two quadrants of the LAOS curves to obtain a stress deconstruction for the complete cycle. In this paper, quadrants I and IV were chosen for analysis.

2. Shear reversal experiments

To conduct an LAOS shear reversal experiment, we identify points of interest on the Lissajous–Bowditch curve each defined by a specific instantaneous strain, strain rate pair $(\gamma, \dot{\gamma})$. At each point of interest, the strain rate was abruptly reversed from $\dot{\gamma}$ to a continuous constant strain rate of $-\dot{\gamma}$. The measurement results from this protocol for $(\gamma = 3.57, \dot{\gamma} = 0.7 \text{ s}^{-1})$ and $(\gamma = -3.57, \dot{\gamma} = 0.7 \text{ s}^{-1})$ are shown in Figs. 2(a) and 2(b) for quadrants I and IV of the Lissajous–Bowditch curves, respectively.

In each figure, we plot the instantaneous strain (γ) , strain rate $(\dot{\gamma})$, stress (σ) , and viscosity (η) versus time (t) through two LAOS cycles (unshaded region) followed by a reversal experiment (shaded region). The roman numerals above the topmost plot indicate the quadrant of the Lissajous curve at that time period. The system was initially sheared for approximately two full cycles, which was sufficient for achieving

reproducible LAOS behavior. At the time of reversal, t_{rev} , the strain and strain rate abruptly changes from the LAOS oscillatory behavior to a steady state shear with a strain rate equal in magnitude but in the opposite direction. Simultaneously, the stress and viscosity exhibit drops characteristic of reversal experiments in shear-thickening fluids [37].

3. Shear cessation experiments

The cessation experiment was implemented in a similar manner as the reversal experiment, with the instantaneous strain rate being set to zero upon reaching the selected point of interest. The measurement results from this protocol for $(\gamma = 3.57, \dot{\gamma} = 0.7 \text{ s}^{-1})$ and $(\gamma = -3.57, \dot{\gamma} = 0.7 \text{ s}^{-1})$ are shown in Figs. 2(c) and 2(d) for quadrants I and IV of the Lissajous–Bowditch curves, respectively.

Similar to the shear reversal experiment, we plot in each figure the instantaneous strain (γ) , strain rate $(\dot{\gamma})$, stress (σ) , and viscosity (η) versus time (t) through two LAOS cycles (unshaded region) followed by a cessation experiment (shaded region). The roman numerals above the topmost plot indicate the quadrant of the Lissajous curve at that time period. The system was sheared for approximately two full cycles, which was sufficient for achieving reproducible LAOS behavior. At the time of cessation, t_{ces} , the instantaneous strain and strain rate transition from the LAOS time-periodic behavior to a zero-shear stress relaxation regime. Simultaneously, the stress exhibits a rapid exponential decay characteristic of cessation experiments in shear-thickening

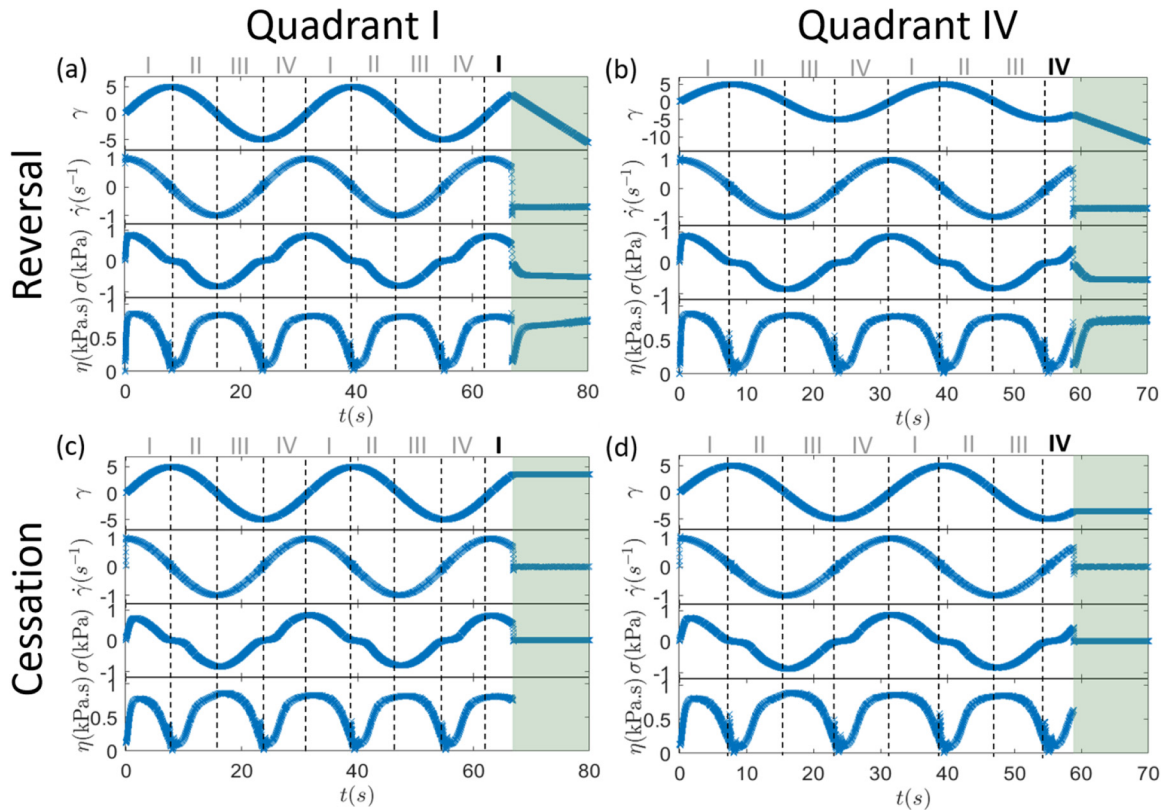


FIG. 2. Plots of instantaneous strain (γ) , strain rate $(\dot{\gamma})$, stress (σ) , and viscosity (η) versus time for (a) and (b) reversal experiments in quadrant I and IV and (c) and (d) cessation experiments in quadrants I and IV. The roman numerals on top of each plot correspond to the quadrant of the Lissajous curve at that time period. The grayed region near the end of each plot shows the period after reversal or cessation. Viscosities are not shown after shear cessation since the instantaneous strain rate is zero.

fluids [41,47–49]. The suspension viscosity is not shown after t_{ces} since the strain rate is zero.

IV. MEASUREMENT RESULTS

To determine the relative contributions of the contact, Brownian, and hydrodynamic stresses, we conduct shear reversal and shear cessation experiments for different points across the LAOS cycle. Prior to each set of reversal and cessation experiment, the sample was sheared for 2 min at a constant shear rate of 0.5 s^{-1} to recreate the same initial condition. The exact protocol can be found in the supplementary material [51].

A. Quadrant I

We implement a reversal experiment as described in Fig. 2(a) and extract the relationship between the stresses before and after reversal. We plot the total stress σ versus

strain after reversal $\gamma(t_{\text{rev}}) - \gamma$ in Fig. 3(a). Each color indicates data for a specific instantaneous strain rate chosen on the Lissajous–Bowditch curve. For clarity, datasets at only five strain rates are shown in the figure. The dashed lines indicate the stress measured just prior to reversal on the Lissajous curve, σ_T , and the open circle corresponds to the stress at the lowest measurable strain postreversal, σ_{rev} . For each dataset, the difference between each dashed line and the open circle gives $\sigma_T - \sigma_{\text{rev}} = \sigma_C + 2\sigma_B$. We note that since higher shear rates have been applied to the suspension during the LAOS cycle, this protocol results in a higher stress during LAOS (dashed lines) than at steady state after reversal.

We implement a cessation experiment as depicted in Fig. 2(c) to extract the Brownian stress. We plot the total stress after cessation versus time in Fig. 3(b), where we have set $t = 0 \text{ s}$ to be the point of cessation. Different color curves

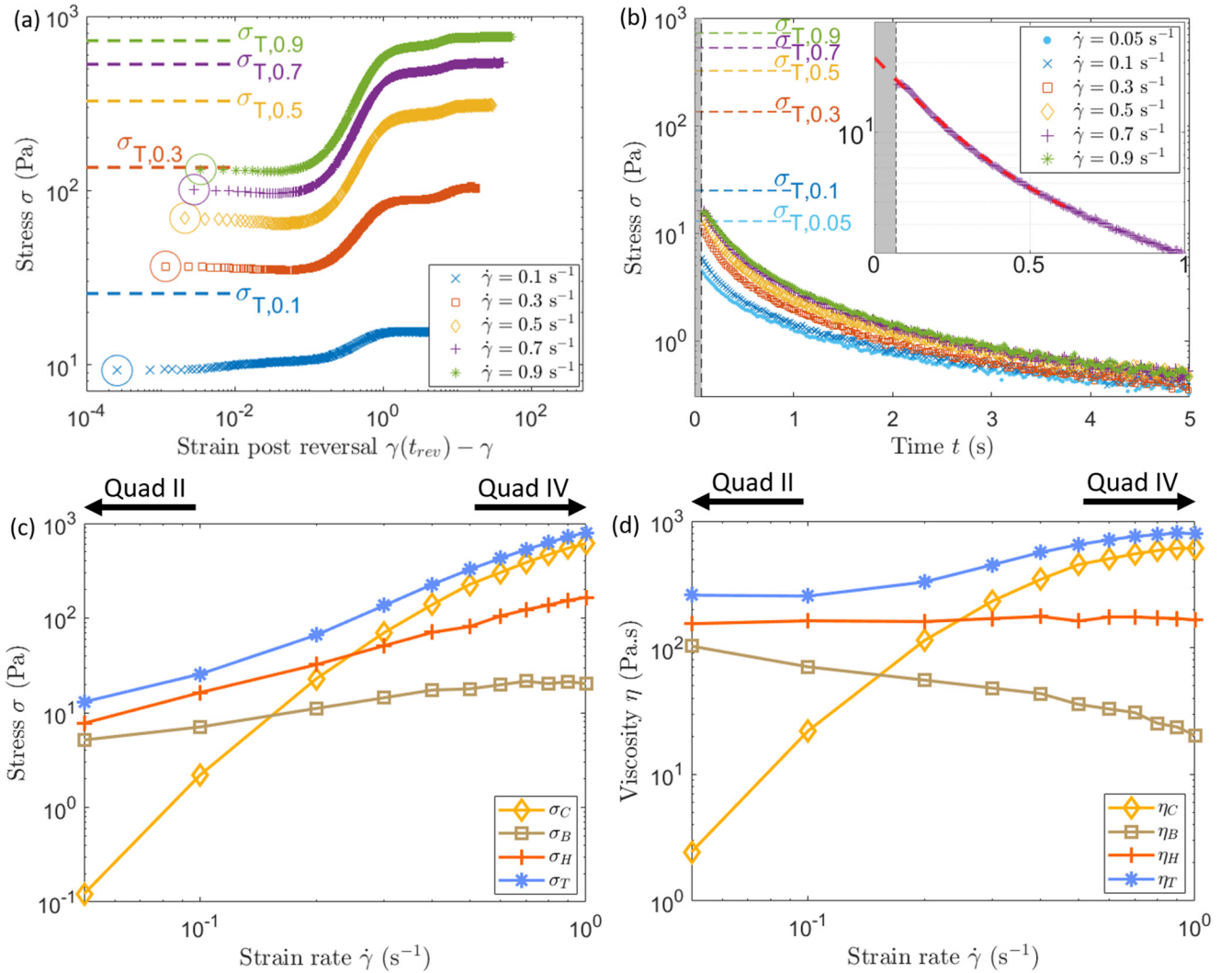


FIG. 3. Results from reversal and cessation experiments in quadrant I of the Lissajous curve. (a) Stress versus strain post reversal curves for the shear reversal experiment. $\gamma(t_{\text{rev}})$ corresponds to the strain at the time of reversal, and the open circles correspond to the first measurable stress after reversal. (b) Stress versus time curves for the shear cessation experiment, where $t = 0 \text{ s}$ corresponds to the time of cessation. The gray area corresponds to the region where instrument inertia significantly affects the data and is excluded from our analysis. The inset shows an exponential fit (red dashed curve) to the data corresponding to an instantaneous shear rate of 0.7 s^{-1} . The Brownian stress is extracted by extrapolating the red fit to $t = 0 \text{ s}$. For clarity, the density of data points plotted has been reduced. Different color curves represent different instantaneous strain rate $\dot{\gamma}$ on the Lissajous–Bowditch curve for both (a) and (b). (c) Decomposed stress against instantaneous strain rate using the proposed protocol and (d) is the corresponding viscosity versus strain rate curve. The subscripts C, B, H, and T represent the contact, Brownian, hydrodynamic, and total stress/viscosity, respectively.

distinguish between data from different instantaneous strain rates on the Lissajous–Bowditch curve, while the dashed lines indicate the total stress before cessation for each of these strain rates. The shaded region near $t = 0$ s is significantly affected by instrument inertia effects, and data in this region are, therefore, not shown and excluded from our analysis. The inset shows an exponential fit in red to the data for the instantaneous strain rate of 0.7 s^{-1} in purple. The Brownian stress was extracted by extrapolating the fit to $t = 0$ s. Only the first 600 ms of the data was fitted as we are interested in the initial Brownian response at $t = 0$ s. In this manner, we determine the Brownian stress for each of the instantaneous strain rates.

We complete the stress decomposition by combining the results from both the reversal and cessation experiments [Figs. 3(a) and 3(b)]. From Eqs. (1) and (2) and the measured Brownian stress, we extract the contact, Brownian, and

hydrodynamic stresses and plot them along with the total stress against instantaneous strain rate in Fig. 3(c).

Finally, we determine the viscosity contributions due to contact, Brownian, and hydrodynamic stresses in Fig. 3(d). Moving clockwise along the LAOS curve, these data show that at high instantaneous strain rates, where the suspension behaves as a Newtonian fluid with a shear-thickened viscosity [top left region of quadrant I in Fig. 1(a)], the suspension response is dominated by the contact stresses. For the chosen LAOS amplitude, the viscosity due to contacts is larger than the hydrodynamic viscosity by a factor of five and larger than the Brownian viscosity by a factor of 30. At lower instantaneous strain rates [right region of quadrant I in Fig. 1(a)], the suspension viscosity decreases. The viscosity decomposition indicates that while the hydrodynamic viscosity remains nearly constant, the viscosity contribution arising from contact stresses diminishes by more than two orders of

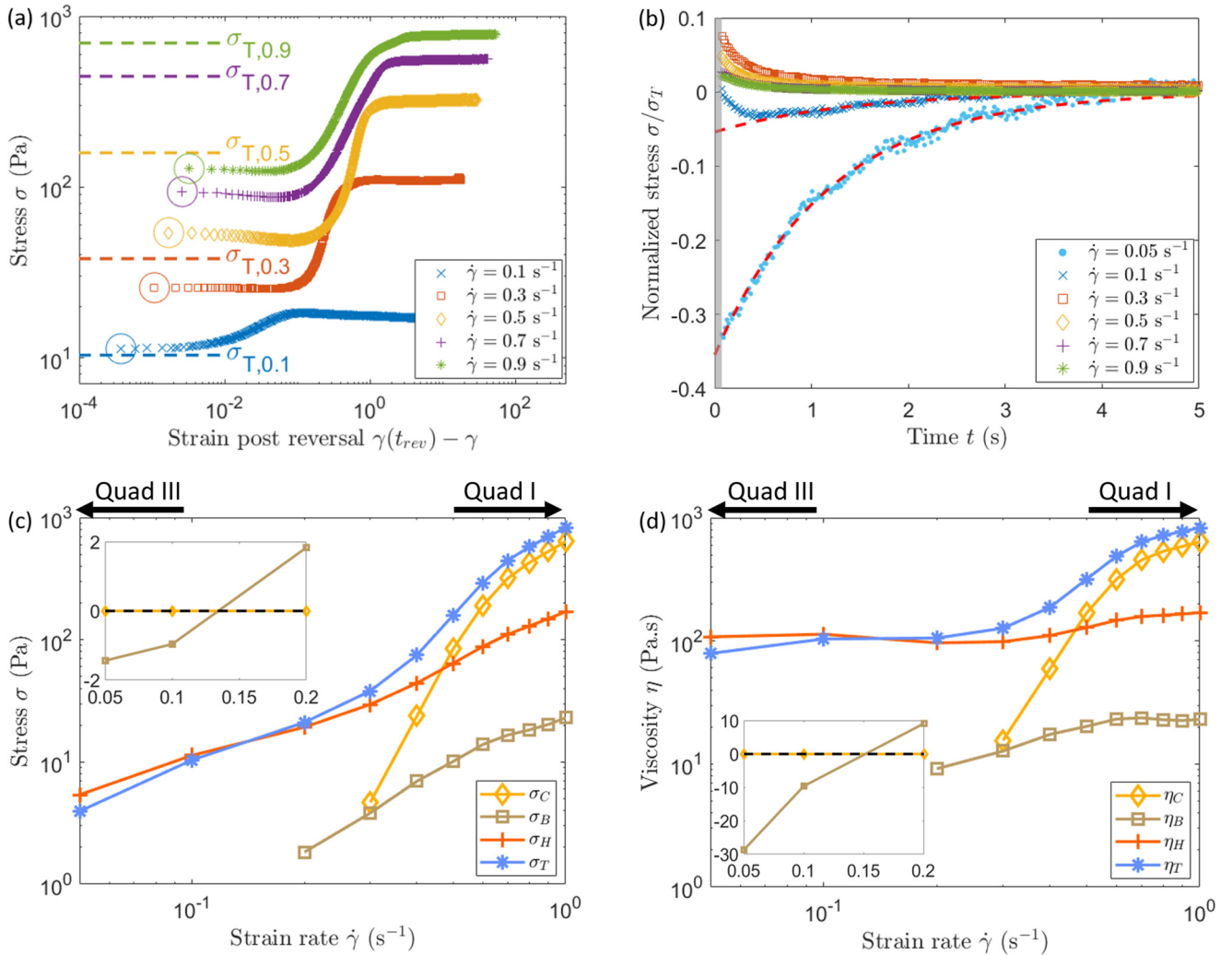


FIG. 4. Reversal and cessation experiment in quadrant IV of the Lissajous curve. (a) Stress versus strain curves for the shear reversal experiment. $\gamma(t_{rev})$ corresponds to the strain at the time of reversal, and the open circles correspond to the first measurable stress after reversal. (b) Stress versus time curves for the shear cessation experiment where $t = 0$ s corresponds to the time of cessation. The density of the data points plotted has been reduced. Different color curves represent different instantaneous strain rate $\dot{\gamma}$ on the Lissajous–Bowditch curve for both (a) and (b). (c) Decomposed stress versus instantaneous strain rate curve and (d) the corresponding viscosity versus instantaneous strain rate curve. The subscripts C, B, H, and T represent the contact, Brownian, hydrodynamic, and total stress/viscosity, respectively. Data for $\dot{\gamma} \leq 0.2 \text{ s}^{-1}$ are calculated based on the assumption that $\sigma_C = 0$. Negative contributions to the stresses and viscosities are shown in the insets on a linear scale.

magnitude, whereas the Brownian viscosity increases by almost an order of magnitude.

B. Quadrant IV

We implement a reversal experiment as described in Fig. 2(b) and extract the relationship between the stresses before and after reversal. We plot the total stress σ versus strain after reversal, $\gamma(t_{\text{rev}}) - \gamma$, in Fig. 4(a). In addition, we indicate with dashed lines the stress measured just prior to reversal, with the colors, once again, indicating the LAOS instantaneous strain rates analyzed. Using the same protocol, we take σ_{rev} to be the stress value at the lowest measurable strain after reversal (open circles). The difference between each dashed line and the left-most stress value for its corresponding curve gives $\sigma_T - \sigma_{\text{rev}}$. We note that the suspension has not had sufficient time to reach steady state during LAOS. Thus, the stresses during LAOS (dashed lines) are smaller than the steady state shear after reversal.

We implement a cessation experiment as described in Fig. 2(d) to extract the Brownian stress. We plot the normalized stress versus time in Fig. 4(b) with $t = 0$ s set as the point of cessation. Different curve colors indicate different LAOS instantaneous strain rates prior to cessation. We find that for the higher strain rate curves associated with the thickening behavior in quadrant IV, the Brownian stress is positive (against the instantaneous shear direction) and decays with time as was observed in the previous analysis for quadrant I. For the $\dot{\gamma} < 0.2 \text{ s}^{-1}$ data, we find that the Brownian stress is negative (along the instantaneous shear direction) and decays with time. As before, we determine the Brownian stress at the point of cessation via exponential fits to the data, with the fits shown in red for the $\dot{\gamma} = 0.05 \text{ s}^{-1}$ and $\dot{\gamma} = 0.1 \text{ s}^{-1}$ data. In this manner, we determine the Brownian stress for each instantaneous strain rate.

We complete the stress decomposition by combining the results from both the reversal and cessation experiments [Figs. 4(a) and 4(b)]. For $\dot{\gamma} > 0.2 \text{ s}^{-1}$, we use Eqs. (1) and (2), and the measured Brownian stress to extract the contact, Brownian, and hydrodynamic stresses and plot them along with the total stress in Fig. 4(c).

For $\dot{\gamma} \leq 0.2 \text{ s}^{-1}$, the protocol must be modified. The negative Brownian stresses at these LAOS instantaneous strain rates suggest that the suspension microstructure has memory of the shear history in quadrant III. Physically, this negative stress likely stems from the suspension having just undergone a reversal within the LAOS cycle itself and having insufficient time for the microstructure to rearrange. The presence of this residual microstructure reduces the strain required after reversal for shear thickening to arise, as shown in Fig. 4(a). The finite time response of the rheometer, which gives rise to finite strain accumulated prior to our measurement of σ_{rev} , thus prevents us from accurately recovering the stress immediately after reversal for $\dot{\gamma} \leq 0.2 \text{ s}^{-1}$ as the finite strain accumulated may induce contact stresses in σ_{rev} . This is consistent with the observation that $\sigma_{\text{rev}} > \sigma_T$ for $\dot{\gamma} = 0.1 \text{ s}^{-1}$ as shown in Fig. 4(a). As such, it is necessary to modify our interpretation of our data.

Since the system has just undergone reversal in the LAOS cycle, we can assume that contact stresses are negligible [37]. If that is the case, Eq. (1) simplifies to $\sigma_T = \sigma_B + \sigma_H$. From this equation and the measured Brownian stress, we can extract the hydrodynamic stress for these points in the LAOS curve [Fig. 4(c)].

Finally, we determine the viscosity contributions due to contact, Brownian, and hydrodynamic stresses in Fig. 4(d). Moving clockwise along the LAOS curve, these data show that at low instantaneous strain rates [left region of quadrant IV in Fig. 1(a)], the contribution from hydrodynamic stresses dominates the contact and Brownian response.

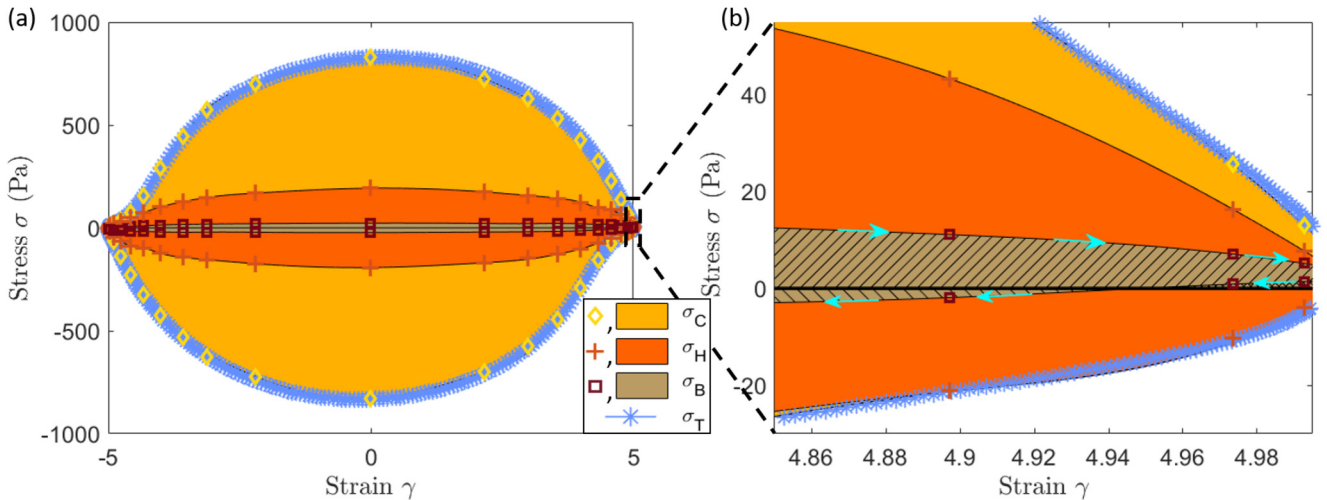


FIG. 5. Visualization of the relative contribution of each stress component at different points on the Lissajous–Bowditch curve. The relative stress contribution is indicated by the colored area, superimposed on the Lissajous–Bowditch curve. The contact stress σ_C is represented in yellow beneath the diamond markers, the hydrodynamic stress σ_H is represented in orange beneath the plus markers, and the Brownian stress σ_B is represented in brown beneath the square markers. The colored areas are generated via spline interpolation based on the markers plotted over each curve. (b) A magnified view of the region near the LAOS reversal. The cyan arrows indicate the direction of strain on the bounding curve which sandwiches the Brownian contribution area with the bold black zero stress line. The Brownian contributions have been hatched where the forward slashes indicate contribution in quadrant I and the backslash correspond to quadrant II. The cross-hatched area at the far right corner is to be taken into account for both quadrants.

In this regime, the viscosity due to contacts is minimal, while the viscosity contribution due to Brownian motion is negative and helps drive the suspension flow. As the instantaneous strain rate increases [top right region of quadrant IV in Fig. 1(a)], the suspension shear thickens. This thickening is primarily driven by contact stresses. The hydrodynamic viscosity is nearly constant, which indicates that for this volume fraction, the particle rearrangements do not substantially alter the hydrodynamic stresses. Finally, the Brownian viscosity transitions from a negative value that helps drive the flows, to a positive value that opposes the flows as particles rearrange and pack along the new maximum compressive axis.

V. DISCUSSION

We compile the results from Figs. 3(c) and 4(c) to determine the relative contributions of each stress component to the total LAOS response and plot the result in Fig. 5. The shaded regions represent contributions from the contact stress σ_C (yellow), hydrodynamic stress σ_H (orange), and Brownian stress σ_B (brown). The blue crosses represent the total stress, σ_T . Overall, we find that in the thickened regimes corresponding to the high stresses (near $\gamma = 0$, when the instantaneous strain rates are the highest), the contact contribution to the stress dominates. This behavior is consistent with the prior literature [25,35,37], implicating contact stresses as the primary driver for shear-thickening. More complex behaviors are observed after the LAOS reversal points at the extreme strains. There, for quadrants II and IV, we find that the total stress dips below the hydrodynamic stress and that the Brownian contribution, instead of resisting, helps to drive the flow [Fig. 5(b)]. We interpret this result to mean that the particles concentrated along the maximal compressive axis in the preceding quadrant have not yet rearranged along the new compressive axis. This structural memory also helps elucidate why, in quadrant IV, the onset strain for thickening after reversal is not constant [Fig. 4(a)]. Specifically, for the lower instantaneous strain rates, the suspension requires less strain to thicken after reversal because of this residual structural anisotropy.

VI. CONCLUSION

We have shown that the proposed stress decomposition protocol provides us with an experimental avenue to determine the relative contributions of the contact, Brownian, and hydrodynamic stresses in an LAOS experiment. Collectively, these results substantially aid in the interpretation of LAOS data in dense suspensions and also serve to provide severe constraints for proposed models for the flow.

These particular experiments were conducted in a continuously thickening suspension. For denser suspensions exhibiting discontinuous shear thickening, these protocols may need to be modified. It may also be the case that in this regime, a stress controlled rheometer such as the Anton Paar MCR702 might be a better candidate to accurately impose the required stress to obtain the familiar “S” shape stress versus strain rate curve.

More broadly, large amplitude oscillatory shear is being used more and more frequently to characterize materials ranging from blood to polymer melts, to gels, and even ballistic clays. It is, therefore, worth considering whether additional features such as the stress decomposition illustrated here, as well as other shear protocols [23,50] should be implemented as standard protocols in rheometers [51].

ACKNOWLEDGMENTS

The authors thank Anton Paar for use of the Twin Drive MCR 702 rheometer through their VIP academic research program and the Cohen group for their insightful suggestions. This work is supported by the National Science Foundation (NSF) CBET (Award Nos. 1804963 and 1509308, as well as No. DMR-1507607). E.Y.X.O. is supported by the Agency of Science Technology and Research, Singapore NSF (Ph.D.) award. The complex fluids research in the Non-Newtonian Fluids (NNF) group at MIT is supported by a gift from Procter & Gamble. The authors would like to thank B. Keshavarz and M. Geri for their assistance in implementing these LAOS reversal/cessation protocols on the ARES-G2.

REFERENCES

- [1] Laurati, M., S. U. Egelhaaf, and G. Petekidis, “Plastic rearrangements in colloidal gels investigated by LAOS and LS-Echo,” *J. Rheol.* **58**(5), 1395–1417 (2014).
- [2] Dealy, J. M., and K. F. Wissbrun, *Melt Rheology and its Role in Plastics Processing: Theory and Applications* (Springer Science & Business Media, New York, 2012).
- [3] Rogers, S. A., J. Kohlbrecher, and M. P. Lettinga, “The molecular origin of stress generation in worm-like micelles, using a rheo-SANS LAOS approach,” *Soft. Matter.* **8**(30), 7831–7839 (2012).
- [4] Ng, T. S. K., G. H. McKinley, and R. H. Ewoldt, “Large amplitude oscillatory shear flow of gluten dough: A model power-law gel,” *J. Rheol.* **55**(3), 627–654 (2011).
- [5] Lettinga, M. P., P. Holmqvist, P. Ballesta, S. A. Rogers, D. Kleshchanok, and B. Struth, “Nonlinear behavior of nematic platelet dispersions in shear flow,” *Phys. Rev. Lett.* **109**(24), 246001 (2012).
- [6] Schlatter, G., G. Fleury, and R. Muller, “Fourier transform rheology of branched polyethylene: Experiments and models for assessing the macromolecular architecture,” *Macromolecules* **38**(15), 6492–6503 (2005).
- [7] Klein, C. O., H. W. Spiess, A. Calin, C. Balan, and M. Wilhelm, “Separation of the nonlinear oscillatory response into a superposition of linear, strain hardening, strain softening, and wall slip response,” *Macromolecules* **40**(12), 4250–4259 (2007).
- [8] Neidhöfer, T., M. Wilhelm, and B. Debbaut, “Fourier-transform rheology experiments and finite-element simulations on linear polystyrene solutions,” *J. Rheol.* **47**(6), 1351–1371 (2003).
- [9] Wilhelm, M., D. Maring, and H.-W. Spiess, “Fourier-transform rheology,” *Rheol. Acta* **37**(4), 399–405 (1998).
- [10] Shu, R., W. Sun, T. Wang, C. Wang, X. Liu, and Z. Tong, “Linear and nonlinear viscoelasticity of water-in-oil emulsions: Effect of droplet elasticity,” *Colloids Surf. A Physicochem. Eng. Aspects* **434**, 220–228 (2013).
- [11] Gurmon, A. K., and N. J. Wagner, “Large amplitude oscillatory shear (LAOS) measurements to obtain constitutive equation model parameters: Giesekus model of banding and nonbanding wormlike micelles,” *J. Rheol.* **56**(2), 333–351 (2012).

- [12] Ewoldt, R. H., A. E. Hosoi, and G. H. McKinley, "New measures for characterizing nonlinear viscoelasticity in large amplitude oscillatory shear," *J. Rheol.* **52**(6), 1427–1458 (2008).
- [13] Garinei, A., and E. Pucci, "Constitutive issues associated with LAOS experimental techniques," *J. Rheol.* **60**(4), 705–714 (2016).
- [14] Rogers, S. A., and M. P. Lettinga, "A sequence of physical processes determined and quantified in large-amplitude oscillatory shear (LAOS): Application to theoretical nonlinear models," *J. Rheol.* **56**(1), 1–25 (2012).
- [15] Lee, C.-W., and S. A. Rogers, "A sequence of physical processes quantified in LAOS by continuous local measures," *Korea-Aust. Rheol. J.* **29**(4), 269–279 (2017).
- [16] Dodge, J. S., and I. M. Krieger, "Oscillatory shear of nonlinear fluids I. Preliminary investigation," *Trans. Soc. Rheol.* **15**(4), 589–601 (1971).
- [17] Cho, K. S., K.-W. Song, and G.-S. Chang, "Scaling relations in nonlinear viscoelastic behavior of aqueous PEO solutions under large amplitude oscillatory shear flow," *J. Rheol.* **54**(1), 27–63 (2010).
- [18] Yu, W., P. Wang, and C. Zhou, "General stress decomposition in nonlinear oscillatory shear flow," *J. Rheol.* **53**(1), 215–238 (2009).
- [19] Choi, J., F. Nettesheim, and S. A. Rogers, "The unification of disparate rheological measures in oscillatory shearing," *Phys. Fluids* **31**(7), 073107 (2019).
- [20] Ewoldt, R. H., "Defining nonlinear rheological material functions for oscillatory shear," *J. Rheol.* **57**(1), 177–195 (2013).
- [21] Lee, J. C.-W., Y.-T. Hong, K. M. Weigandt, E. G. Kelley, H. Kong, and S. A. Rogers, "Strain shifts under stress-controlled oscillatory shearing in theoretical, experimental, and structural perspectives: Application to probing zero-shear viscosity," *J. Rheol.* **63**(6), 863–881 (2019).
- [22] Lee, J. C.-W., K. M. Weigandt, E. G. Kelley, and S. A. Rogers, "Structure-property relationships via recovery rheology in viscoelastic materials," *Phys. Rev. Lett.* **122**(24), 248003 (2019).
- [23] Lee, J. C.-W., L. Porcar, and S. A. Rogers, "Recovery rheology via rheo-SANS: Application to step strains under out-of-equilibrium conditions," *AIChE J.* **65**(12), e16797 (2019).
- [24] Brady, J. F., "Brownian motion, hydrodynamics, and the osmotic pressure," *J. Chem. Phys.* **98**(4), 3335–3341 (1993).
- [25] Mari, R., R. Seto, J. F. Morris, and M. M. Denn, "Shear thickening, frictionless and frictional rheologies in non-Brownian suspensions," *J. Rheol.* **58**(6), 1693–1724 (2014).
- [26] Mari, R., R. Seto, J. F. Morris, and M. M. Denn, "Discontinuous shear thickening in Brownian suspensions by dynamic simulation," *Proc. Natl. Acad. Sci. U.S.A.* **112**(50), 15326–15330 (2015).
- [27] Singh, A., R. Mari, M. M. Denn, and J. F. Morris, "A constitutive model for simple shear of dense frictional suspensions," *J. Rheol.* **62**(2), 457–468 (2018).
- [28] Denn, M. M., J. F. Morris, and D. Bonn, "Shear thickening in concentrated suspensions of smooth spheres in newtonian suspending fluids," *Soft Matter* **14**(2), 170–184 (2018).
- [29] Gillissen, J. J. J., and H. J. Wilson, "Modeling sphere suspension microstructure and stress," *Phys. Rev. E* **98**(3), 033119 (2018).
- [30] Ness, C., R. Mari, and M. E. Cates, "Shaken and stirred: Random organization reduces viscosity and dissipation in granular suspensions," *Sci. Adv.* **4**(3), eaar3296 (2018).
- [31] Batchelor, G. K., "The effect of Brownian motion on the bulk stress in a suspension of spherical particles," *J. Fluid. Mech.* **83**(1), 97–117 (1977).
- [32] Batchelor, G. K., and J. Green, "The determination of the bulk stress in a suspension of spherical particles to order c^2 ," *J. Fluid. Mech.* **56**(3), 401–427 (1972).
- [33] Batchelor, G. K., and J.-T. Green, "The hydrodynamic interaction of two small freely-moving spheres in a linear flow field," *J. Fluid Mech.* **56**(2), 375–400 (1972).
- [34] Russel, W. B., "The rheology of suspensions of charged rigid spheres," *J. Fluid Mech.* **85**(2), 209–232 (1978).
- [35] Seto, R., R. Mari, J. F. Morris, and M. M. Denn, "Discontinuous shear thickening of frictional hard-sphere suspensions," *Phys. Rev. Lett.* **111**(21), 218301 (2013).
- [36] James, N. M., E. Han, R. A. L. de la Cruz, J. Jureller, and H. M. Jaeger, "Interparticle hydrogen bonding can elicit shear jamming in dense suspensions," *Nat. Mater.* **17**(11), 965 (2018).
- [37] Lin, N. Y., B. M. Guy, M. Hermes, C. Ness, J. Sun, W. C. Poon, and I. Cohen, "Hydrodynamic and contact contributions to continuous shear thickening in colloidal suspensions," *Phys. Rev. Lett.* **115**(22), 228304 (2015).
- [38] Gadala-Maria, F., and A. Acrivos, "Shear-induced structure in a concentrated suspension of solid spheres," *J. Rheol.* **24**(6), 799–814 (1980).
- [39] Goddard, J. D., "A dissipative anisotropic fluid model for non-colloidal particle dispersions," *J. Fluid Mech.* **568**, 1–17 (2006).
- [40] Mackay, M. E., and B. Kaffashi, "Stress jumps of charged colloidal suspensions, measurement of the elastic-like and viscous-like stress components," *J. Colloid Interface Sci.* **174**(1), 117–123 (1995).
- [41] O'Brien, V. T., and M. E. Mackay, "Stress components and shear thickening of concentrated hard sphere suspensions," *Langmuir* **16**(21), 7931–7938 (2000).
- [42] Kaffashi, B., V. T. O'Brien, M. E. Mackay, and S. M. Underwood, "Elastic-like and viscous-like components of the shear viscosity for nearly hard sphere, Brownian suspensions," *J. Colloid Interface Sci.* **187**(1), 22–28 (1997).
- [43] Watanabe, H., M.-L. Yao, A. Yamagishi, K. Osaki, T. Shitata, H. Niwa, and Y. Morishima, "Nonlinear rheological behavior of a concentrated spherical silica suspension," *Rheol. Acta* **35**(5), 433–445 (1996).
- [44] Westermeier, F., D. Pennicard, H. Hirsemann, U. H. Wagner, C. Rau, H. Graafsma, P. Schall, M. P. Lettinga, and B. Struth, "Connecting structure, dynamics and viscosity in sheared soft colloidal liquids: A medley of anisotropic fluctuations," *Soft Matter* **12**(1), 171–180 (2016).
- [45] Ianni, F., D. Lasne, R. Sarcia, and P. Hébraud, "Relaxation of jammed colloidal suspensions after shear cessation," *Phys. Rev. E* **74**(1), 011401 (2006).
- [46] Mohanty, R. P., and R. N. Zia, "Transient nonlinear microrheology in hydrodynamically interacting colloidal dispersions: Flow cessation," *J. Fluid Mech.* **884**, A14 (2020).
- [47] Maharjan, R., and E. Brown, "Giant deviation of a relaxation time from generalized Newtonian theory in discontinuous shear thickening suspensions," *Phys. Rev. Fluids* **2**(12), 123301 (2017).
- [48] Marenne, S., J. F. Morris, D. R. Foss, and J. F. Brady, "Unsteady shear flows of colloidal hard-sphere suspensions by dynamic simulation," *J. Rheol.* **61**(3), 477–501 (2017).
- [49] Zia, R. N., and J. F. Brady, "Stress development, relaxation, and memory in colloidal dispersions: Transient nonlinear microrheology," *J. Rheol.* **57**(2), 457–492 (2013).
- [50] Lin, N. Y., C. Ness, M. E. Cates, J. Sun, and I. Cohen, "Tunable shear thickening in suspensions," *Proc. Natl. Acad. Sci. U.S.A.* **113**(39), 10774–10778 (2016).
- [51] See supplementary material at <https://doi.org/10.1122/1.5144520> for information on (A) rheometer calibration, (B) MCR 702 measurement data and analysis, (C) time evolution of the LAOS cycle used in this paper, and (D) exact rheometer protocols for both the ARES-G2 and MCR 702.